AIAA 82-4288

Numerical Simulation of Steady Supersonic Flow over Spinning Bodies of Revolution

W. B. Sturek*
U.S. Army Ballistic Research Laboratory/ARRADCOM, Aberdeen Proving Ground, Maryland
and
L. B. Schiff†
NASA Ames Research Center, Moffett Field, California

A recently reported parabolized Navier-Stokes code has been employed to compute the supersonic flowfield about a spinning cone and spinning and nonspinning ogive cylinder and boattailed bodies of revolution at moderate incidence. The computations were performed for flow conditions where extensive measurements for wall pressure, boundary-layer velocity profiles, and Magnus force had been obtained. Comparisons between the computational results and experiment indicate excellent agreement for angles of attack up to 6 deg. At angles greater than 6 deg discrepancies are noted which are tentatively attributed to turbulence modeling errors. The comparisons for Magnus effects show that the code accurately predicts the effects of body shape for the selected models.

Nomenclature

a = speed of sound
c_p = specific heat at constant pressure
C_Y = Magnus- (side-) force coefficient
C_{pw} = wall surface pressure component of Magnus-force coefficient
$C_{\Delta p}$ = centrifugal pressure gradient component of Magnus-force coefficient
$C_{\tau x}$ = longitudinal velocity wall shear component of Magnus-force coefficient
$C_{\tau\phi}$ = circumferential velocity wall shear component of Magnus force
e = total energy per unit volume of fluid, normalized by $\rho_\infty a_\infty^2$
e_i = internal energy, normalized by a_∞^2
$\hat{E}_s, \hat{F}, \hat{G}, \hat{q}$ = flux vectors of transformed gasdynamic equation [Eq. (2)]
J = Jacobian of transformation between physical and computational coordinates
L = reference length
M = Mach number
p = pressure, normalized by $\rho_\infty a_\infty^2$
Pr = Prandtl number, $\mu_\infty c_p/\kappa_\infty$
Re = Reynolds number, $\rho_\infty U_\infty L/\mu_\infty$
$\hat{Re}$ = Reynolds number [Eq. (1)], $\rho_\infty a_\infty L/\mu_\infty$
$\hat{S}$ = viscous flux vector [Eq. (6)]
u, v, w = Cartesian velocity components along the x, y, z axes, respectively, normalized by a_∞
U, V, W = contravariant velocity components [Eq. (3)]
x, y, z = physical Cartesian coordinate axes (Fig. 1)
α = angle of attack
γ = ratio of specific heats
κ = coefficient of thermal conductivity, normalized by freestream value κ_∞
μ = coefficient of viscosity, normalized by freestream value μ_∞
ξ, η, ζ = computational coordinates in the axial, circumferential, and radial directions (Fig. 1)
ρ = density, normalized by freestream density ρ_∞
ϕ = circumferential angle (Fig. 1)
Ω = spin rate about body axis, rpm

Subscripts

∞ = freestream conditions
w = body surface values
x = based on axial distance from nose

Received Oct. 14, 1981; revision received April 2, 1982. This paper is declared a work of the U.S. Government and therefore is in the public domain.

*Aerospace Engineer. Associate Fellow AIAA.
†Research Scientist. Associate Fellow AIAA.

Introduction

THE use of separate, coupled codes for computing inviscid flow and turbulent boundary-layer development over yawed, spinning and nonspinning bodies of revolution has yielded some very good solutions for cone and ogive-cylinder shapes[1]; however, application of these techniques to bodies with boattailed afterbodies has not yielded satisfactory results even at small angle of attack ($\alpha \leq 4$ deg).[1]

Recent publications have reported supersonic flowfield computations using parabolized Navier-Stokes (PNS) techniques. These publications have reported very good results for cone models for laminar and turbulent viscous flow,[2,3] and for cone and ogive-cylinder models for laminar viscous flow.[4,5] The PNS method appears to offer an attractive technique for computing flow over bodies having discontinuities in surface curvature since the inviscid flow and viscous layer are computed simultaneously. Further, the PNS method permits adequate flowfield resolution to be achieved at reasonable computer costs. This paper reports the results of detailed comparisons of PNS computational results to experimental measurements of turbulent boundary-layer profile characteristics of an ogive-cylinder-boattail body, at Mach number = 3. In addition, comparisons are made between the PNS computations, coupled inviscid boundary-layer (INV-BL) computations, and experimental measurements of Magnus forces for cone, ogive-cylinder, and ogive-cylinder-boattail models, at Mach numbers ranging from $M = 2$ to 4. The PNS code employed is the one reported by Schiff and Steger.[6] The coupled inviscid boundary-layer code is that reported by Sturek et al.[1] The INV-BL technique involves separate computations of the inviscid flow, of the viscous boundary-layer development and the effective viscous displacement surface, and of the inviscid flow for the body plus the displacement surface.

Overview of Numerical Scheme

Governing Equations and Numerical Scheme

A body-conforming ξ, η, ζ, coordinate system (Fig. 1) is used which maps the body surface and outer boundary of the flow region in physical space onto coordinate surfaces of the computational space. This transformation simplifies the

application of surface boundary conditions and permits the approximation of neglecting streamwise and circumferential viscous terms in high Reynolds number flow.[6] The resulting nondimensional steady, thin-layer PNS equations can be written in strong conservation-law form as

$$\frac{\partial \hat{E}_s}{\partial \xi} + \frac{\partial \hat{F}}{\partial \eta} + \frac{\partial \hat{G}}{\partial \zeta} = \frac{1}{\hat{Re}} \frac{\partial \hat{S}}{\partial \zeta} \tag{1}$$

where $\xi = \xi(x)$ is the axial (marching) coordinate; $\eta = \eta(x,y,z)$ is the circumferential coordinate; and $\zeta = \zeta(x,y,z)$ is the radial coordinate. The inviscid flux vectors are

$$E_s = J^{-1} \begin{bmatrix} \rho U \\ \rho uU + \xi_x p \\ \rho vU \\ \rho wU \\ (e+p_s)U \end{bmatrix}, \quad F = J^{-1} \begin{bmatrix} \rho V \\ \rho uV + \eta_x p \\ \rho vV + \eta_y p \\ \rho wV + \eta_z p \\ (e+p)V \end{bmatrix}$$

$$G = J^{-1} \begin{bmatrix} \rho W \\ \rho uW + \zeta_x p \\ \rho vW + \zeta_y p \\ \rho wW + \zeta_z p \\ (e+p)W \end{bmatrix} \tag{2}$$

with contravariant velocity components

$$U = \xi_x u \quad V = \eta_x u + \eta_y v + \eta_z w \quad W = \zeta_x u + \zeta_y v + \zeta_z w \tag{3}$$

The internal energy of the gas e_i is defined in terms of the conservative variables as

$$e_i = (e/\rho) - 0.5(u^2 + v^2 + w^2) \tag{4}$$

where for a perfect gas

$$p/\rho = (\gamma - 1)e_i = a^2/\gamma \tag{5}$$

The thin-layer model viscous terms, valid for high Reynolds number flow and body-conforming coordinates are

$$\hat{S} = J^{-1} \begin{bmatrix} 0 \\ \mu(\zeta_x^2 + \zeta_y^2 + \zeta_z^2)u_\zeta + (\mu/3)(\zeta_x u_\zeta + \zeta_y v_\zeta + \zeta_z w_\zeta)\zeta_x \\ \mu(\zeta_x^2 + \zeta_y^2 + \zeta_z^2)v_\zeta + (\mu/3)(\zeta_x u_\zeta + \zeta_y v_\zeta + \zeta_z w_\zeta)\zeta_y \\ \mu(\zeta_x^2 + \zeta_y^2 + \zeta_z^2)w_\zeta + (\mu/3)(\zeta_x u_\zeta + \zeta_y v_\zeta + \zeta_z w_\zeta)\zeta_z \\ \{(\zeta_x^2 + \zeta_y^2 + \zeta_z^2)[(\mu/2)(u^2 + v^2 + w^2)_\zeta \\ + \kappa Pr^{-1}(\gamma - 1)^{-1}(a^2)_\zeta] + (\mu/3)(\zeta_x u \\ + \zeta_y v + \zeta_z w)(\zeta_x u_\zeta + \zeta_y v_\zeta + \zeta_z w_\zeta)\} \end{bmatrix} \tag{6}$$

For turbulent flow the coefficients of molecular viscosity and thermal conductivity appearing in Eq. (6) are calculated using the two-layer model reported by Baldwin and Lomax[7] where the constants within the model were set to the values suggested in Ref. 7, with the exception that the turbulent Prandtl number Pr_t was set to 0.8.

Equation (1) is parabolic-like with resepct to ξ and can be marched downstream in the ξ direction from an initial data plane (subject to appropriate body and freestream boundary conditions), under those conditions where the local flow is supersonic. By evaluating the pressure p_s which appears in the $\hat{E}_s$ flux vector using the subsonic layer approximation, Eq. (1) is also stable for subsonic marching. If p_s is set equal to the local pressure for supersonic points, and is evaluated from $\partial p_s/\partial \zeta = 0$ for points within the subsonic viscous layer adjacent to a wall, Eq. (1) can be marched for all flows where $u > 0$; that is, for flows without streamwise reversal (see Ref. 6 for associated stability analysis).

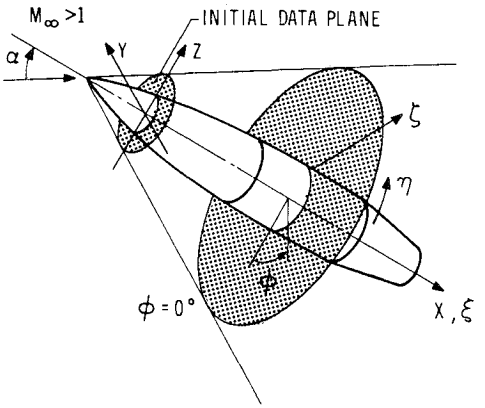

Fig. 1 Coordinates and notation.

The numerical algorithm used to advance Eq. (1) downstream in ξ is a noniterative, implicit, approximately-factored finite difference scheme, analogous to the one developed by Beam and Warming[8] for the solution of the unsteady Navier-Stokes equations. The algorithm can be written in so-called delta form as[6]

$$\begin{aligned} &[\tilde{A}_s^j + (1-\alpha)\Delta\xi(\delta_\eta \tilde{B}^j)](\tilde{A}_s^j)^{-1}[\tilde{A}_s^j + (1-\alpha)\Delta\xi(\delta_\zeta \tilde{C}^j \\ &\quad - \hat{Re}^{-1}\delta_\zeta \tilde{M}^j)]\Delta\hat{q}^j = -(\tilde{A}_s^j - \tilde{A}_s^{j-1})\hat{q}^j + \alpha(\hat{E}_s^j - \hat{E}_s^{j-1}) \\ &\quad - (1-\alpha)\Delta\xi\{\delta_\eta[\eta_x^{j+1}(E/J)^j + \eta_y^{j+1}(F/J)^j \\ &\quad + \eta_z^{j+1}(G/J)^j] + \delta_\zeta[\zeta_x^{j+1}(E/J)^j + \zeta_y^{j+1}(F/J)^j \\ &\quad + \zeta_z^{j+1}(G/J)^j] - \hat{Re}^{-1}\delta_\zeta \tilde{S}^j\} - [(\xi_x/J)^{j+1}E_p^j \\ &\quad - (\xi_x/J)^j E_p^{j-1}] + \mathfrak{D}\hat{q}^j \end{aligned} \tag{7}$$

where $\hat{q} = J^{-1}(\rho, \rho u, \rho v, \rho w, e)$ and $\mathfrak{D}$ is the fourth-order numerical damping term.

The algorithm is conservative, of second-order accuracy in the marching direction, and can be either second- or fourth-order accurate in the cross flow plane. A fully implicit technique is employed to impose the wall boundary conditions consisting of the no slip condition for the velocity components and either fixed or adiabatic wall temperature. The algorithm has been applied to a variety of laminar and turbulent flows resulting in excellent agreement with those obtained from more costly time-dependent computations.

Conical Initial Solutions

In general the initial data plane for the marching method must be supplied from an auxiliary computation. However, when treating the flow over conical or pointed bodies, the marching code can be used to generate its own initial data plane.[6] The solution is marched downstream from an initial station using a conical grid and, after each step, the solution is scaled to place it back at the original station. When no change in the flow variables occur with further marching, the variables are constant along rays, and a conical solution has been generated. If the flow variables within the viscous layer can also be assumed to be locally constant along rays, the same procedure can be used to generate viscous conical

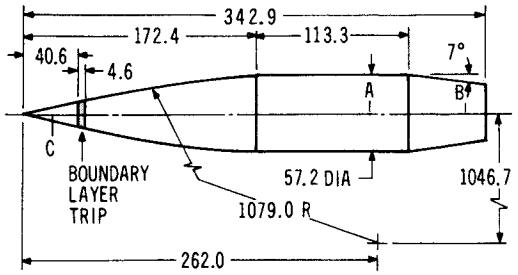

NOTE: DIMENSIONS ARE IN MILLIMETRES
A,B BOUNDARY LAYER SURVEY STATIONS
C CONICAL STARTING SOLUTION STATION

Fig. 2 Ogive-cylinder-boattail model dimensions.

solutions. A discussion of the applicability of the conical viscous assumption is found in Refs. 6 and 9.

For the ogive-cylinder-boattail computations, the tip of the ogive was replaced with a cone tangent to the ogive at $x=0.267$ cal. Conical solutions were generated at that station and used as starting data for the marching code. A small error is made in generating the starting solution with the conical approximation for cases with surface spin due to the change in circumferential velocity with longitudinal position. However, this error is small since the step size used in the conical initial solution is less than 1% of the distance from the tip to the initial data plane. In any event, this error quickly decays as the initial solution is marched over the body.

Viscous Resolution

A strategy for moving the grid was developed for the PNS code in order to maintain adequate resolution of the viscous layer as the solution develops over the full length of the spinning model. This capability was also found to be of importance in maintaining computational stability, particularly for the computations made at Mach number = 4. The strategy employed was to check for the value of $y^+ (y^+ = \rho_w U_\tau y/\mu_w;\ U_\tau = \sqrt{\tau_w/\rho_w})$ at the first grid point above the model surface and to adjust the grid stretching parameters to maintain this value of y^+ within the desired range, $5 \le y^+ \le 10$. If the value of y^+ was found to be outside the specified criteria, the stretching parameter was adjusted by 0.5% for the next computational step. Although the technique works well in general, it was found that permitting too great a change in the grid configuration from step to step resulted in the introduction of errors into the computation.

Results

Model Geometry and Experimental Measurements

The dimensions of the ogive-cylinder-boattail model used for the detailed flowfield studies are shown in Fig. 2. The model closely resembles a modern low-drag artillery projectile and is 6-calibers long with a 1-caliber long, 7-deg boattail. Experimental data available include wall static pressure,[10] turbulent boundary-layer velocity profiles,[11,12] wall skin friction,[11] and flow visualization. The test conditions were $M=3$ with a tunnel total pressure of 0.298 MPa and tunnel total temperature of 308 K. These conditions resulted in a freestream Reynolds number of 7.3×10^6 based on the model length. The boundary layer was tripped near the tip of the model to produce turbulent flow. Additionally, aerodynamic force measurements[13,14] were available for 10-deg cone, ogive-cylinder and ogive-cylinder-boattail shapes at $M=2$, 3, and 4. These data include Magnus and pitch plane aerodynamic force and moment coefficients. All tests were performed using SSWT No. One at the U. S. Army Ballistic Research Laboratory. This facility, which is no longer in operation, was a continuous flow tunnel with a flexible plate nozzle. The test section size was 330×380 mm (13×15 in.).

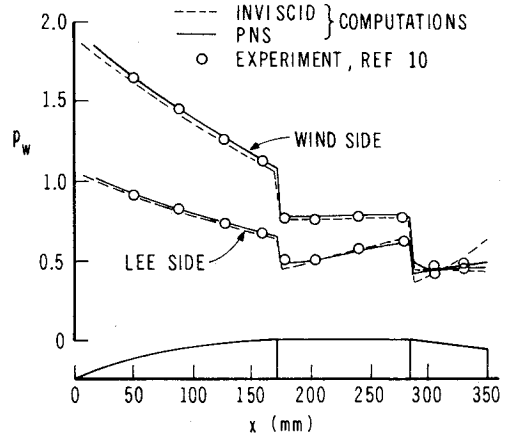

Fig. 3 Axial surface pressure distribution on ogive-cylinder-boattail body; $M=3.0$, $\alpha=6.3$ deg, $Re_\infty=2.13\times10^7$/m.

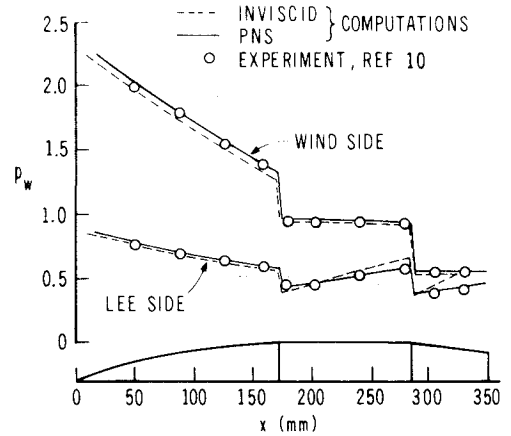

Fig. 4 Axial surface pressure distribution on ogive-cylinder-boattail body; $M=3.0$, $\alpha=10.4$ deg, $Re_\infty=2.13\times10^7$/m.

PNS Computations and Code Performance

The computations presented here resulted from a large number of numerical runs in which the step size, grid spacing, and smoothing constants were varied widely. The step size Δx was varied from 0.30 to 0.76 mm without significant changes being observed in the solution. The most critical variable is the grid resolution of the viscous layer. The present computations used a grid consisting of 36 equispaced circumferential points ($\Delta\phi=10$ deg) and 50 points radially between the body and the outer boundary. Computation time on a CDC 7600 computer is 2.3 s/(marching station) with this size grid.

Comparison Between Computation and Flowfield Measurements

Surface Pressure

The PNS computations are compared to experimental measurements, and to inviscid flow computations made using codes based on MacCormack's predictor-corrector technique (Figs. 3-6).[15,16] Longitudinal surface pressure distributions along the windward and leeward rays of the nonspinning body are shown in Figs. 3 and 4 for angles of attack of 6.3 deg and 10.4 deg, respectively. The PNS and inviscid computations are both in excellent agreement with experimental measurements for angles of attack up to and including 4.2 deg (not shown). However, it is of interest to note that the PNS computations exhibit consistently better agreement with experiment in the vicinity of the discontinuities in streamwise surface curvature which occur at the ogive-cylinder and cylinder-boattail junctions. At $\alpha=6.3$ deg (Fig. 3) the PNS computation exhibits good agreement with the experimental

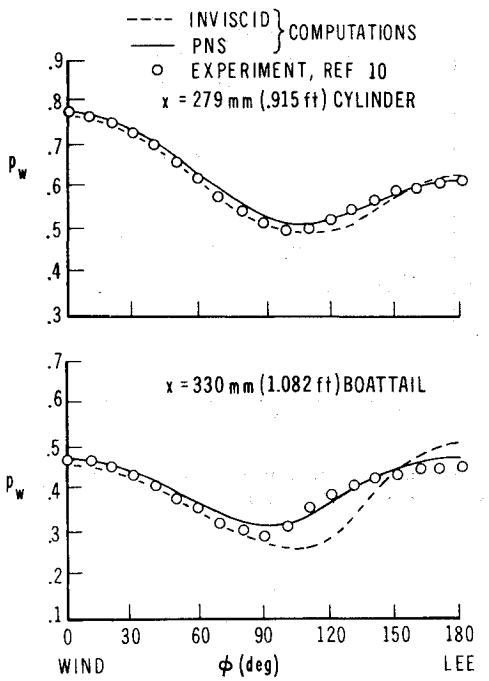

Fig. 5 Circumferential surface pressure distributions; $M=3.0$, $\alpha=6.3$ deg, $Re_\infty=2.13\times10^7$/m.

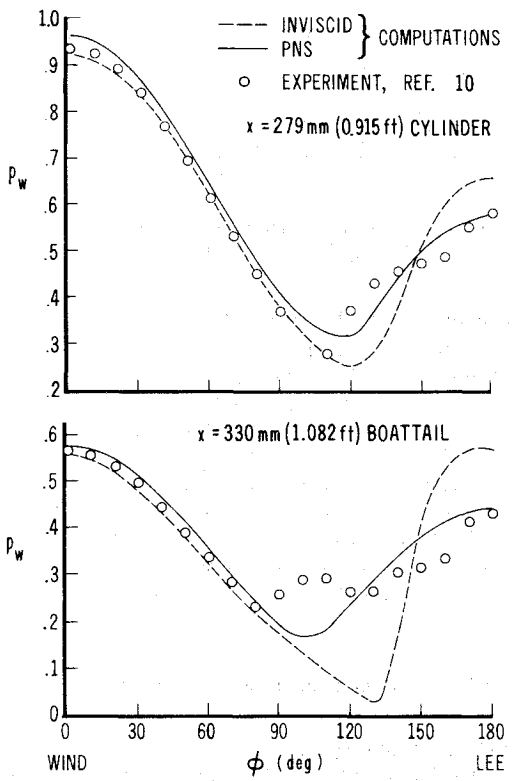

Fig. 6 Circumferential surface pressure distributions; $M=3.0$, $\alpha=10.4$ deg, $Re_\infty=2.13\times10^7$/m.

measurements, while the inviscid computation indicates a discrepancy on the leeward side of the boattail. The discrepancy is attributed to the strong viscous interaction caused by the appearance of cross-flow separation and rollup of leeward-side vortices in the vicinity of the boattail. As the angle of attack is increased further the cross-flow separation region extends progressively farther forward along the body. At $\alpha=10.4$ deg (Fig. 4) the PNS computation exhibits good agreement with the experimental measurements, while the

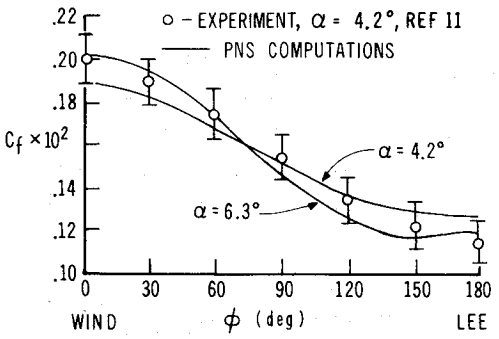

Fig. 7 Circumferential skin-friction coefficient distributions; $M=3.0$, $X=254$ mm, $Re_x=5.41\times10^6$.

inviscid results deviate from the experiment on the leeward side of both the cylinder and the boattail.

The appearance of a cross-flow separation region is further indicated by the circumferential surface pressure distributions. Examples of comparisons of these distributions are shown for $\alpha=6.3$ deg in Fig. 5 and for $\alpha=10.4$ deg in Fig. 6 at two longitudinal stations; one on the cylinder portion of the model near the boattail, the second, midway on the boattail. Computational results and experimental measurements have been obtained for circumferential stations ranging completely around the body. At low angles of attack the flowfield about the nonspinning body has left-right symmetry about the pitch plane, thus only circumferential stations on one half of the body are shown. At $\alpha=4.2$ deg such comparisons (not shown) indicated uniformly good agreement between both computations and the experiment for all body stations. At $\alpha=6.3$ deg the comparison on the cylinder (Fig. 5) indicates excellent agreement between the PNS computation and experiment and the appearance of a systematic discrepancy between the inviscid computation and experiment for $100\leq\phi\leq150$ deg. This trend is accentuated for flow on the boattail (Fig. 5). The comparison shown in Fig. 6 for $\alpha=10.4$ deg indicates further development of a cross-flow separation for flow over the boattail and cylinder. The abrupt rise in experimental surface pressure at $\phi\simeq90$ deg indicates the location of the cross-flow separation point. The inviscid computation predicts a cross-flow shock at $\phi\simeq140$ deg which is not present in the experimental data. At this incidence the PNS computation is in only fair agreement with the experiment and suggests an upper limit of applicability of the present computational technique of $\alpha=6$ deg for this class of body shapes.

Skin Friction

An example of results obtained for the skin-friction coefficient is shown in Fig. 7 for a fixed longitudinal station on the cylinder near the boattail at circumferential stations around the body. Computed results for $\alpha=4.2$ deg are shown and are compared with Preston tube measurements made at that incidence. The computed skin-friction values for $\alpha=4.2$ deg are less than the experimental ones on the windward side and greater than experiment on the leeward side of the body; however, the comparison is within the expected experimental uncertainty of $\pm15\%$ (the error bars in Fig. 7 indicate ±0.001 C_f which is approximately $\pm10\%$). In addition, computed results for $\alpha=6.3$ deg are shown in Fig. 7 which illustrate a shift in trend of the computed skin-friction coefficient with increasing incidence. At $\alpha=6.3$ deg the minimum value of C_f is reached at $\phi=150$ deg as opposed to $\phi=180$ deg as in the $\alpha=4.2$-deg case. This is a further indication of the developing leeward-side vortical structure with increasing incidence previously shown in the pressure distributions.

Streamwise Velocity Profiles

A more sensitive test of the accuracy of the PNS computational technique applied to this flow is the comparison of

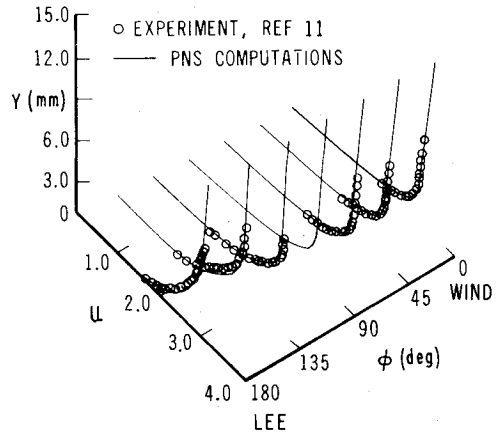

Fig. 8 Boundary-layer velocity profiles on ogive-cylinder-boattail body; $M=3.0$, $\alpha=6.3$ deg, $Re_\infty=2.13\times10^7$/m, $X=254$ mm, cylinder.

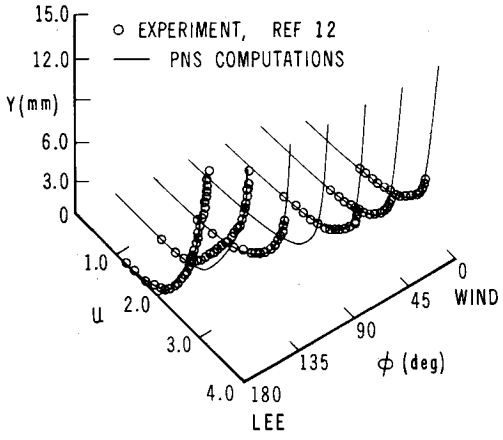

Fig. 9 Boundary-layer velocity profiles on ogive-cylinder-boattail body; $M=3.0$, $\alpha=6.3$ deg, $Re_\infty=2.13\times10^7$/m, $X=324$ mm, boattail.

measured and computed boundary-layer velocity profiles. Such comparisons are shown in Figs. 8-10 for two longitudinal stations; station A on the cylinder near the boattail, and station B on the boattail (see Fig. 2). Each figure shows the velocity profiles for a particular longitudinal station at circumferential stations ranging from the windward to leeward ray in 30-deg increments. The nondimensional streamwise velocity components u are plotted vs physical distance y measured radially from the body surface in millimeters, rather than against normalized y/δ. This method of plotting prevents scaling differences between the computation and experiment from giving a false comparison.

Comparisons made for $\alpha=4.2$ deg for both spinning[17] and nonspinning[9] bodies (not shown) demonstrate a generally good agreement between the measured and computed velocity profiles. However, a slight discrepancy was observed for the profile at $\phi=150$ deg (and 210 deg), 30 deg displaced from the leeward plane. Similar comparisons for $\alpha=6.3$ deg are shown in Figs. 8 and 9. At this angle of attack the windward side measured and computed profiles are still in excellent agreement. However, the discrepancy between the profiles at $\phi=150$ deg is substantial, particularly at the boattail station (Fig. 9). Note that this discrepancy is less strongly reflected in the surface pressure distribution at the corresponding station (Fig. 5).

To assess the relative roles of circumferential pressure gradients vs the expansion over the boattail as the source of the discrepancy in the velocity profiles, a comparison was also made at $\alpha=6.3$ deg for a body with a straight cylindrical afterbody replacing the boattail. This comparison is shown in

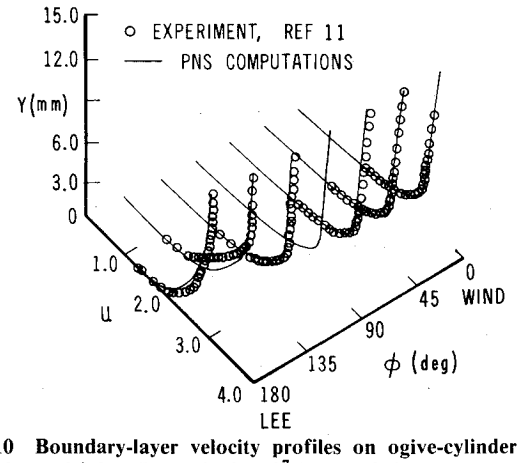

Fig. 10 Boundary-layer velocity profiles on ogive-cylinder body; $M=3.0$, $\alpha=6.3$ deg, $Re_\infty=2.13\times10^7$/m, $X=318$ mm.

Fig. 10 at a longitudinal station comparable to that of the boattail. The computational overprediction of streamwise velocity at $\phi=150$ deg, observed for the boattailed body, is also present for the cylindrical body. This result suggests that the main source of the discrepancy is not flow expansion over the boattail, but rather is linked to the development of the leeward-side vortex structure.

Circumferential Velocity

The surface pressure and streamwise velocity profile distributions indicate that a discrepancy exists between the computational and experimental results in the cross-flow separation region. At $\alpha=4.2$ deg good agreement is observed between the computed and measured data. At $\alpha=6.3$ deg a discrepancy is observed in the streamwise velocity profiles on the leeward side of the body, but is not evident as yet in the surface pressure distributions. As the angle of attack increases, the leeward side vortex structure becomes stronger and extends further along the body. Thus at $\alpha=10.4$ deg, a substantial difference is observed between the computed and the measured surface pressure distributions on the leeward side of the body (velocity profiles were not measured at this angle of attack). This discrepancy is also evidenced in the computed results for the cross-flow velocity vectors. Figure 11 shows the projections of the computed velocity vectors onto the cross-flow plane (i.e., a plane normal to the body axis of symmetry) located at $x=324$ mm, on the boattail, for an angle of attack of 10.4 deg. At this angle of attack, cross-flow separation (characterized by circumferential flow from the leeward to the windward side of the body) is observed at this longitudinal station. The cross-flow separation angle ϕ_s is obtained from interpolation of the computed circumferential velocity just above the body surface. At this angle of attack the cross-flow separation angle is determined to be $\phi_s=117$ deg, and is shown in Fig. 11.

An experimental vapor-screen flow visualization photo[18] of the leeward-side vortices on the boattail at $\alpha=10.4$ deg is shown in Fig. 12. In the vapor-screen technique water vapor is introduced into the wind tunnel to produce a fog in the test section. A thin, intense plane of light, oriented normal to the body axis of symmetry at a longitudinal station midway along the boattail illuminates the fog. The leeward-side vortices are visible as dark regions within the light plane.

Although the present numerical technique allows the prediction of cross-flow separation, it is obvious that substantial discrepancies between the computation and experiment develop at angles of attack greater than 6 deg. The reason or reasons for this limitation are not known for certain; potential sources include the neglect of circumferential viscous terms within the thin-layer viscous model, and uncertainties in three-dimensional turbulence modeling. However, it is of interest to note that McRae and Hussaini,[19]

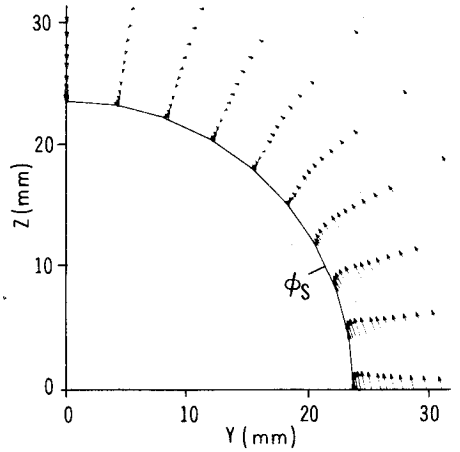

Fig. 11 Cross-flow plane velocity vectors on boattail; $M=3.0$, $\alpha=10.4$ deg, $Re_\infty=2.13\times10^7$/m, $X=324$ mm.

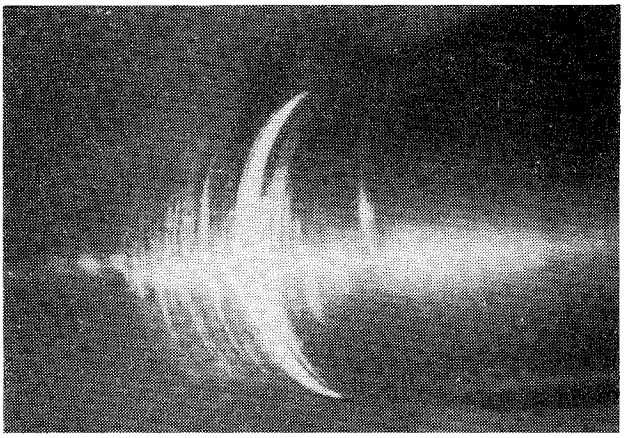

Fig. 12 Vapor-screen flow visualization on boattail; $M=3.0$, $\alpha=10.4$ deg, $Re_\infty=2.13\times10^7$/m.

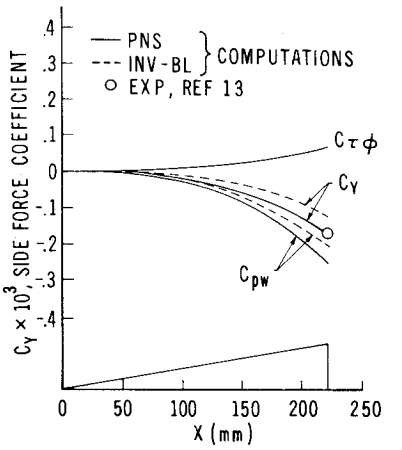

Fig. 13 Magnus-force coefficient for 10-deg cone; $M=3.0$, $\alpha=2$ deg, $\Omega=20$ K rpm, $Re_\infty=2.35\times10^7$/m, turbulent boundary layer.

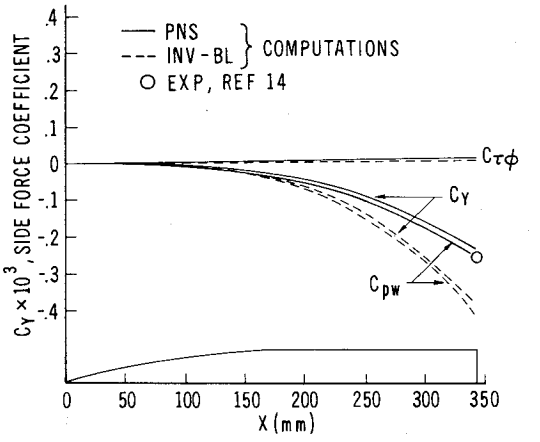

Fig. 14 Magnus-force coefficient for ogive-cylinder body; $M=3.0$, $\alpha=2$ deg, $\Omega=20$ K rpm, $Re_\infty=2.11\times10^7$/m, turbulent boundary layer.

who used a numerical technique which retains the circumferential viscous terms and employs a similar eddy-viscosity model in a study of turbulent cone flows at large incidence, also found significant discrepancies within the cross-flow separation region. In their study, the discrepancies were reduced by modifying the eddy-viscosity turbulence model in the separated region. Rakich et al.[4] reported similar behavior for flow over cones.

Comparison Between Computation and Experiment: Magnus Force and Moment

The Magnus effect is strongly dependent on the circumferential pressure distributions and the asymmetries about the pitch plane that occur when the model is spinning. Thus, the PNS technique is particularly attractive for computations of the Magnus effect since, as seen in Figs. 3-6, the accuracy of the circumferential and longitudinal distributions of surface pressure is much improved over that obtained using inviscid techniques. This improvement was most significant for the flow over the boattail. In order to test the accuracy of the PNS code for computing Magnus effects, several test cases have been run for flow conditions where experimental measurements of Magnus forces and moments have been accomplished.[13,14]

The results of these computations for the 10-deg cone model are shown in Fig. 13 and for the ogive cylinder and ogive-cylinder-boattail models in Figs. 14 and 15, respectively. The individual components of the Magnus effect are plotted vs axial position for Mach = 3, $\alpha=2$ deg; and $\Omega=20$ K rpm.

In Figs. 13-15, comparisons are shown of PNS and INV-BL results for the individual components of the Magnus effect. The results for $C_{\tau\phi}$ (circumferential wall shear component) obtained with the two computational techniques are seen to be in excellent agreement. Good agreement is also indicated for C_{pw} (wall pressure component of the Magnus effect) between the two computational techniques. For the INV-BL technique, the component plotted as C_{pw} is the sum of the wall pressure and centrifugal pressure gradient contributions. This sum is equivalent to the surface pressure contribution determined by the PNS code since in the PNS technique the viscous and inviscid flow are computed simultaneously.

The lines in Figs. 13-15 identified as C_Y represent the total Magnus effect. For the cone (Fig. 13), both the PNS and INV-BL techniques achieve good agreement with the experiment. Corresponding results for the ogive cylinder are shown in Fig. 14. Considering the small magnitude of the Magnus force, the agreement with experiment shown in Fig. 14 for the ogive-cylinder model is considered to be quite good for the INV-BL technique; however, the PNS result is obviously better. This result is also considered to be verification of the INV-BL concept at small angle of attack. The results shown in Fig. 15 for the ogive-cylinder-boattail model show a dramatic superiority of the PNS technique compared to the INV-BL technique. In this case the INV-BL technique greatly exaggerates the effect of the flow over the boattail.

Comparisons of the PNS computations to experiment were carried out for additional Mach number flow conditions

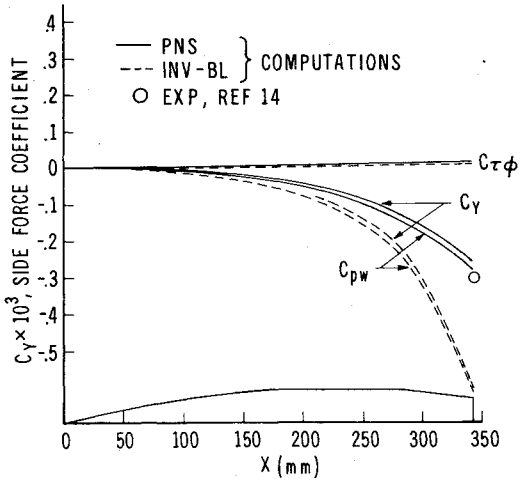

Fig. 15 Magnus-force coefficient for ogive-cylinder-boattail body; $M=3.0$, $\alpha=2$ deg, $\Omega=20$ K rpm, $Re_\infty=2.11\times10^7$/m, turbulent boundary layer.

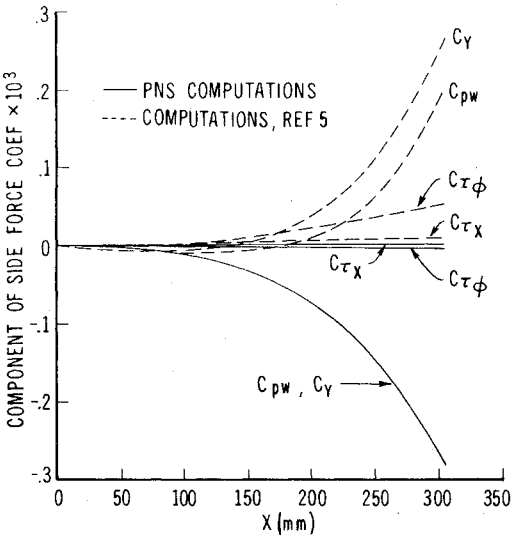

Fig. 16 Magnus-force coefficient for 10-deg cone; $M=4.0$, $\alpha=2$ deg, $\Omega=30$ K rpm, $T_w/T_0=0.24$, $Re_\infty=2.81\times10^6$/m; laminar boundary layer.

$(2\leq M\leq 4)$ for the ogive cylinder and ogive-cylinder-boattail models. The results for the Magnus-force coefficient and for the slope of the Magnus-moment coefficient (not shown, see Ref. 17) indicate excellent agreement for magnitude and for trend with Mach number and body configuration.

Computations have also been performed using the PNS code for laminar viscous flow over a spinning 10-deg cone at $M=4$, $\alpha=2$ deg, $\Omega=30$ K rpm, $T_w/T_0=0.24$. A constant wall temperature boundary condition was included in the PNS code for this computation. Earlier viscous computations for this case, reported in Ref. 5, indicated the presence of a reversed Magnus effect. Individual components of the side force coefficient due to the Magnus effect, obtained with both computational methods, are shown in Fig. 16. The results differ considerably. In contrast to the results of Ref. 5, which show a reversal of the wall pressure component and total Magnus force with increasing body length, the present PNS results vary monotonically with body length. [Note that in Ref. 5 values of $C_{\tau x}$ and C_Y are given only at $x=304.8$ mm (1.0 ft). The intermediate values shown in Fig. 16 were obtained by assuming a linear variation of $C_{\tau x}$ with body length and summing the individual components $C_{\tau x}$, $C_{\tau\phi}$, and C_{pw} to obtain C_Y.] Additional computations were made for a wide

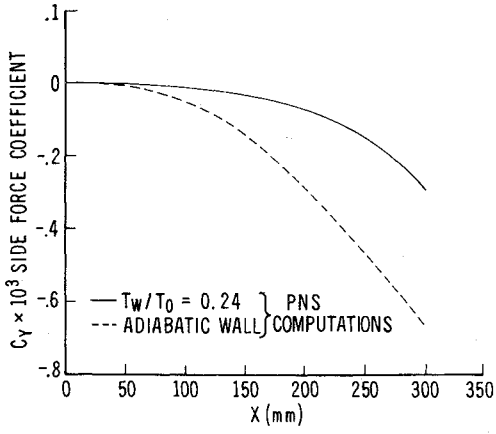

Fig. 17 Magnus-force coefficient for 10-deg cone; $M=4.0$, $\alpha=2$ deg, $\Omega=30$ K rpm, $Re_\infty=2.81\times10^6$/m; laminar boundary layer.

range of grid configurations and the results evidenced no reversal of the Magnus force. The monotonic behavior of the present PNS results for this laminar case follows the classical trend, and is similar to that shown earlier for the turbulent case.

The results of an investigation of the effect of wall temperature are shown in Fig. 17, where computations for a cold wall and adiabatic wall boundary conditions are compared. No tendency for a reversal of the Magnus force was obtained. The effect of the cold wall is to reduce the magnitude of the Magnus force.

Concluding Remarks

This paper has described the results of a numerical computational study in which the parabolized Navier-Stokes marching code recently developed by Schiff and Steger has been exercised for cone, ogive cylinder, and ogive-cylinder-boattail shapes at incidence. Extensive, detailed comparisons to experimental data at $M=3$, $\alpha\leq10.4$ deg have been performed to evaluate the accuracy and stability of the numerical technique.

Comparisons have been made showing excellent agreement between computation and experiment for surface pressures at angles of attack up to 6.3 deg. At an angle of attack of 10.4 deg, the comparison is degraded due to the inability to accurately model the significant leeward-side vortex flow. Excellent agreement is also achieved for velocity profiles. At an angle of attack of 6.3 deg, the agreement is good with the exception of the $\phi=150$-deg circumferential station. Again, this is attributed to the inability to model accurately the developing leeward-side vortex flow. The precise cause of the inaccuracy has not been determined; however, three-dimensional turbulence modeling and inclusion of circumferential viscous terms have been identified as areas for further investigation.

Excellent agreement between computational and experimental results for Magnus force were achieved for spinning cone, ogive cylinder, and boattailed shapes for turbulent viscous flow. These results indicate that the PNS code employed in this study represents a viable computational tool for predicting Magnus effects for spinning projectiles at small angle of attack.

Although this computation technique appears, as a result of this study, to be limited to $\alpha\leq6$ deg for this class of bodies, the computed results do show a significant improvement in capability compared to techniques that compute inviscid flow and viscous effects separately. This increase in capability is achieved without any significant increase in computation cost or requirement for computer resources greater than those currently available with the CDC 7600 computer.

References

[1] Sturek, W. B., Dwyer, H. A., Kayser, L. D., Nietubicz, C. J., Reklis, R. P., and Opalka, K. O., "Computations of Magnus Effects for a Yawed, Spinning Body of Revolution," *AIAA Journal,* Vol. 16, July 1978, pp. 687-692.

[2] Lin, T. C. and Rubin, S. G., "Viscous Flow Over a Cone at Moderate Incidence: I Hypersonic Tip Region," *Computers and Fluids,* Vol. 1, 1973, pp. 37-57.

[3] Lubard, S. C. and Helliwell, W. S., "Calculation of the Flow on a Cone at High Angle of Attack," *AIAA Journal,* Vol. 12, July 1974, pp. 965-974.

[4] Rakich, J. V., Vigneron, Y. C., and Agarwal, R., "Computation of Supersonic Viscous Flows Over Ogive-Cylinders at Angle of Attack," AIAA Paper 79-0131, Jan. 1979.

[5] Agarwal, R. and Rakich, J. V., "Hypersonic Laminar Viscous Flow Past Spinning Cones at Angle of Attack," *AIAA Journal,* Vol. 20, April 1982, pp. 479-486.

[6] Schiff, L. B. and Steger, J. L., "Numerical Simulation of Steady Supersonic Viscous Flow," *AIAA Journal,* Vol. 18, Dec. 1980, pp. 1421-1430.

[7] Baldwin, B. S. and Lomax, H., "Thin Layer Approximation and Algebraic Model for Separated Turbulent Flows," AIAA Paper 78-257, Jan. 1978.

[8] Beam, R. and Warming, R. F., "An Implicit Factored Scheme for the Compressible Navier-Stokes Equations," *AIAA Journal,* Vol. 16, April 1978, pp. 393-402.

[9] Schiff, L. B. and Sturek, W. B., "Numerical Simulation of Steady Supersonic Flow Over an Ogive-Cylinder-Boattail Body," AIAA Paper 80-0066, Jan. 1980.

[10] Reklis, R. P. and Sturek, W. B., "Surface Pressure Measurements on Slender Bodies at Angle of Attack in Supersonic Flow," U. S. Army Ballistic Research Laboratory/ARRADCOM Memo. Rept. ARBRL-MR-02876, Aberdeen Proving Ground, Md., ADA064097, Nov. 1978.

[11] Kayser, L. D. and Sturek, W. B., "Experimental Measurements in the Turbulent Boundary Layer of a Yawed, Spinning Ogive-Cylinder Body of Revolution at Mach 3.0. Part II: Data Tabulation," U. S. Army Ballistic Research Laboratory/ARRADCOM Memo. Rept. ARBRL-MR-02813, Aberdeen Proving Ground, Md., ADA053458, March 1978.

[12] Kayser, L. D. and Sturek, W. B., "Turbulent Boundary Layer Measurements on the Boattail Section of a Yawed, Spinning Projectile Shape at Mach 3.0," U. S. Army Ballistic Research Laboratory/ARRADCOM Memo. Rept. ARBRL-MR-02880, Aberdeen Proving Ground, Md., AD065355, Nov. 1978.

[13] Sturek, W. B., "Boundary Layer Studies on a Spinning Cone," U. S. Army Ballistic Research Laboratory/ARRADCOM Rept. BRL-R-1649, Aberdeen Proving Ground, Md., AD 762564, May 1973.

[14] Nietubicz, C. J. and Opalka, K., "Supersonic Wind Tunnel Measurements of Static and Magnus Aerodynamic Coefficients for Projectile Shapes with Tangent and Secant Ogive Noses," U. S. Army Ballistic Research Laboratory/ARRADCOM Memo. Rept. ARBRL-MR-02991, Aberdeen Proving Ground, Md., ADA083297, Feb. 1980.

[15] Schiff, L. B., "Nonlinear Aerodynamics of Bodies of Coning Motion," *AIAA Journal,* Vol. 10, Nov. 1972, pp. 1517-1522.

[16] Sanders, B. R. and Dwyer, H. A., "Magnus Forces on Spinning Supersonic Cones, Part II: The Inviscid Flow," *AIAA Journal,* Vol. 14, May 1976, pp. 576-582.

[17] Sturek, W. B. and Schiff, L. B., "Computations of the Magnus Effect for Slender Bodies in Supersonic Flow," *Proceedings of the AIAA Atmospheric Flight Mechanics Conference,* Aug. 1980, pp. 260-270.

[18] Nietubicz, C. J., unpublished BRL Wind Tunnel Data, private communication, 1979.

[19] McRae, D. S. and Hussaini, M. Y., "Numerical Simulation of Supersonic Cone Flow at High Angle of Attack," AGARD-CP-247, Jan. 1979.

U.S. POSTAL SERVICE

STATEMENT OF OWNERSHIP, MANAGEMENT AND CIRCULATION

(Required by 39 U.S.C. 3685)

1. TITLE OF PUBLICATION	A. PUBLICATION NO	2. DATE OF FILING
AIAA JOURNAL	0 0 9 9 2 0	Oct. 1,1982
3. FREQUENCY OF ISSUE	A. NO. OF ISSUES PUBLISHED ANNUALLY	B. ANNUAL SUBSCRIPTION PRICE
MONTHLY	12	$14.50

4. COMPLETE MAILING ADDRESS OF KNOWN OFFICE OF PUBLICATION *(Street, City, County, State and ZIP Code) (Not printers)*

1290 AVENUE OF THE AMERICAS, NEW YORK, N.Y. 10104

5. COMPLETE MAILING ADDRESS OF THE HEADQUARTERS OR GENERAL BUSINESS OFFICES OF THE PUBLISHERS *(Not printers)*

SAME AS ABOVE

6. FULL NAMES AND COMPLETE MAILING ADDRESS OF PUBLISHER, EDITOR, AND MANAGING EDITOR *(This item MUST NOT be blank)*

PUBLISHER *(Name and Complete Mailing Address)*

AMERICAN INSTITUTE OF AERONAUTICS AND ASTRONAUTICS, INC. SAME AS ABOVE

EDITOR *(Name and Complete Mailing Address)*

GEORGE W. SUTTON SAME AS ABOVE

MANAGING EDITOR *(Name and Complete Mailing Address)*

ELAINE J. CAMHI SAME AS ABOVE

7. OWNER *(If owned by a corporation, its name and address must be stated and also immediately thereunder the names and addresses of stockholders owning or holding 1 percent or more of total amount of stock. If not owned by a corporation, the names and addresses of the individual owners must be given. If owned by a partnership or other unincorporated firm, its name and address, as well as that of each individual must be given. If the publication is published by a nonprofit organization, its name and address must be stated.) (Item must be completed)*

FULL NAME	COMPLETE MAILING ADDRESS
AMERICAN INSTITUTE OF AERONAUTICS AND ASTRONAUTICS, INC.	SAME AS ABOVE

8. KNOWN BONDHOLDERS, MORTGAGEES, AND OTHER SECURITY HOLDERS OWNING OR HOLDING 1 PERCENT OR MORE OF TOTAL AMOUNT OF BONDS, MORTGAGES OR OTHER SECURITIES *(If there are none, so state)*

FULL NAME	COMPLETE MAILING ADDRESS
NONE	

9. FOR COMPLETION BY NONPROFIT ORGANIZATIONS AUTHORIZED TO MAIL AT SPECIAL RATES *(Section 411.3, DMM only)*
The purpose, function, and nonprofit status of this organization and the exempt status for Federal income tax purposes *(Check one)*

☒ (1) HAS NOT CHANGED DURING PRECEDING 12 MONTHS ☐ (2) HAS CHANGED DURING PRECEDING 12 MONTHS *(If changed, publisher must submit explanation of change with this statement.)*

10. EXTENT AND NATURE OF CIRCULATION	AVERAGE NO. COPIES EACH ISSUE DURING PRECEDING 12 MONTHS	ACTUAL NO. COPIES OF SINGLE ISSUE PUBLISHED NEAREST TO FILING DATE
A. TOTAL NO. COPIES *(Net Press Run)*	5734	5900
B. PAID CIRCULATION 1. SALES THROUGH DEALERS AND CARRIERS, STREET VENDORS AND COUNTER SALES	----	----
2. MAIL SUBSCRIPTION	5205	5387
C. TOTAL PAID CIRCULATION *(Sum of 10B1 and 10B2)*	5205	5387
D. FREE DISTRIBUTION BY MAIL, CARRIER OR OTHER MEANS SAMPLES, COMPLIMENTARY, AND OTHER FREE COPIES	74	73
E. TOTAL DISTRIBUTION *(Sum of C and D)*	5279	5460
F. COPIES NOT DISTRIBUTED 1. OFFICE USE, LEFT OVER, UNACCOUNTED, SPOILED AFTER PRINTING	455	440
2. RETURN FROM NEWS AGENTS	----	----
G. TOTAL *(Sum of E, F1 and 2 - should equal net press run shown in A)*	5734	5900

11. I certify that the statements made by me above are correct and complete

SIGNATURE AND TITLE OF EDITOR, PUBLISHER, BUSINESS MANAGER, OR OWNER

NELSON W. FRIEDMAN, ADMINISTRATOR, MANAGEMENT SYSTEMS

PS Form June 1980 3526 (Page 1) *(See instruction on reverse)*